MATERIALS SCIENCE

A skin-like two-dimensionally pixelized full-color quantum dot photodetector

Jaehyun Kim[1], Sung-Min Kwon[1], Yeo Kyung Kang[2], Yong-Hoon Kim[3], Myung-Jae Lee[4], Kwangjoon Han[5], Antonio Facchetti[6,7], Myung-Gil Kim[3]*, Sung Kyu Park[1]*

Direct full-color photodetectors without sophisticated color filters and interferometric optics have attracted considerable attention for widespread applications. However, difficulties of combining various multispectral semiconductors and improving photon transfer efficiency for high-performance optoelectronic devices have impeded the translation of these platforms into practical realization. Here, we report a low-temperature (<150°C) fabricated two-dimensionally pixelized full-color photodetector by using monolithic integration of various-sized colloidal quantum dots (QDs) and amorphous indium-gallium-zinc-oxide semiconductors. By introducing trap-reduced chelating chalcometallate ligands, highly efficient charge carrier transport and photoresistor-free fine-patterning of QD layers were successfully realized, exhibiting extremely high photodetectivity (>4.2×10^{17} Jones) and photoresponsivity (>8.3×10^3 A W^{-1}) in a broad range of wavelengths (365 to 1310 nm). On the basis of these technologies, a wavelength discriminable phototransistor circuit array (>600 phototransistors) was implemented on a skin-like soft platform, which is expected to be a versatile and scalable approach for wide spectral image sensors and human-oriented biological devices.

INTRODUCTION

An integrated full-color [ultraviolet (UV)–to–infrared (IR)] photodetector fabricated on a skin-like soft platform may offer the collection of meaningful information from a body and the surrounding environment, enabling forthcoming human-oriented technologies such as neuromorphic image sensors (1), soft robotics (2), and biological health monitoring (3). In addition, when addressing complex monitoring targets and environmental conditions, two-dimensional full-color photodetection on a single platform may have a considerable advantage compared to single- or narrow-band photodetection for target discrimination and acquisition of more reliable and extensive information (4). Conventional and recently reported photodetection systems, however, are mostly composed of a simple combination of individual photodetectors, which can only detect a specific or limited range of wavelength, resulting in low pixel resolution, limited tunability of bandwidth, and a complex device architecture (5). In addition, the difficulty of integrating high-resolution multilayered photosensing materials and device arrays for full-color range photodetection with monolithic integration has been a serious impediment for the realization of highly responsive and full-color discriminable skin-like photodetectors arrays (6).

For these reasons, there have been enormous efforts to develop photodetectors with new photosensing materials and device architectures for broadband photodetection, such as colloidal quantum dots (QDs) (7), amorphous oxide semiconductors (AOSs) (8), organic semiconductors (9), perovskite materials (10), and two-dimensional materials (graphene and transition metal dichalcogenides) (11). In particular, for maximizing the photosensitivity in a broadband range,

hybrid device architectures of photodetectors have been largely pursued (12, 13). For example, graphene-QDs (4), MoS$_2$-graphene (14), AOSs-QDs (15), and organic-carbon nanotube photodetectors (16) have been reported, demonstrating high gains and optical sensitivities as a result of combining semiconductors with distinct optoelectronic and charge transport properties. However, although the previous advances are noteworthy, they typically presented a narrow-band absorbing material with limited bandgap tunability and wavelength-discriminating ability (17). To overcome these limitations, particularly in terms of photosensitivity, full-color photodetection, and wavelength discrimination, colloidal QDs have attracted considerable attention for their unique optoelectronic characteristics such as a wide bandgap tunability and high light absorption coefficients (18, 19). In addition, for large-area and active-matrix driving of the photodetectors, AOSs such as amorphous indium-gallium-zinc-oxide (a-IGZO)–based thin-film transistors (TFTs) have been actively investigated owing to their high carrier mobility, low off-state current, and scalability (20). Despite the interesting proprieties of colloidal QDs and a-IGZO, their monolithic integration for highly sensitive full-color photodetection has been rarely reported, mainly due to several issues (15, 17), particularly (i) the optimization of QD/a-IGZO photodetector architecture for full-color photodetection and wavelength discrimination, (ii) the realization of a complementary metal-oxide semiconductor (CMOS)–compatible high-resolution patterning of multi-QD layers for a large-area and skin-like multiplexing array, and (iii) the poor control of the QD/a-IGZO interface to achieve a highly efficient charge transfer.

Here, we report a versatile and large-area scalable approach to extend the detection bandwidth of a photodetector from UV to IR, using monolithic integration of QDs with a-IGZO phototransistors and implementing a low-temperature fabricated two-dimensional in-pixel charge integrating circuit (CIC) array for color discrimination. In particular, by introducing an electrically high-performance and trap-reduced chelating chalcometallate ligand for the QDs, ultrahigh photodetectivity (4.2×10^{17} Jones) was achieved, which is a record in the best solution-processed organic and QD devices so far. In addition, a high-resolution patterning of multiple QD layers via a direct photopatterning and their pixelized phototransistors are demonstrated for a

[1]Displays and Devices Research Lab. School of Electrical and Electronics Engineering, Chung-Ang University, Seoul 06974, Korea. [2]Department of Chemistry, Chung-Ang University, Seoul 06974, Korea. [3]School of Advanced Materials Science and Engineering, Sungkyunkwan University, Suwon 16419, Korea. [4]Division of Nano and Energy Convergence Research, Daegu Gyeongbuk Institute of Science and Technology (DGIST), 333, Techno Jungang Daero, Hyeonpung-Myeon, Dalseong-Gun, Daegu 42988, Korea. [5]Hyundai Motor Group R&D Division, Hwaseong-si, 18280, Korea. [6]Department of Chemistry and the Materials Research Center, Northwestern University, 2145 Sheridan Road, Evanston, IL 60208, USA. [7]Flexterra Corporation, 8025 Lamon Avenue, Skokie, IL 60077, USA.
*Corresponding author. Email: skpark@cau.ac.kr (S.K.P.); bombmg@gmail.com (M.-G.K.)

skin-like two-dimensional photodetector that is capable of position-dependent full-color photodetection.

RESULTS AND DISCUSSION
Device structure and operation mechanism
To realize full-color photodetection with high sensitivity, two strategies have been carried out; first, the photodetector architecture and the in-pixel circuit were designed for high sensitivity, and second, monolithic integration of QDs with an a-IGZO active layer and interfacial control for full-color light absorption and highly efficient charge collection were optimized. Recently, three-terminal photodetector devices such as a phototransistor have been extensively investigated since they outperform the conventional photodiodes in terms of photosensitivity, external quantum efficiency (EQE), and a sublinear responsivity to

irradiance, especially at low intensities (*13*, *21*). Therefore, the high photosensitivity and the sublinear responsivity of the phototransistors enable a wide dynamic range operation, particularly when arrayed with pixelized schemes for image sensors and two-dimensional large-area applications. Figure 1A shows the schematic device and array structures of a flexible QD/a-IGZO photodetector fabricated on an ultrathin polyimide (PI) substrate (see the Supplementary Materials for detailed fabrication procedure). The cross-sectional high-resolution transmission electron microscope (HRTEM) images confirm the stacking of QDs on the a-IGZO layer and also the uniform distribution of the QD layer (Fig. 1, D to F). For detection of the light for full-color range, various QD layers having different bandgaps, particularly PbS QDs (10 nm diameter; bandgap, 0.95 eV), CdSe QDs (7 and 5 nm diameter; bandgaps, 1.95 and 2.39 eV, respectively), and CdS QDs (3 nm diameter; bandgap, 3.07 eV), were separately formed on the a-IGZO layer in a
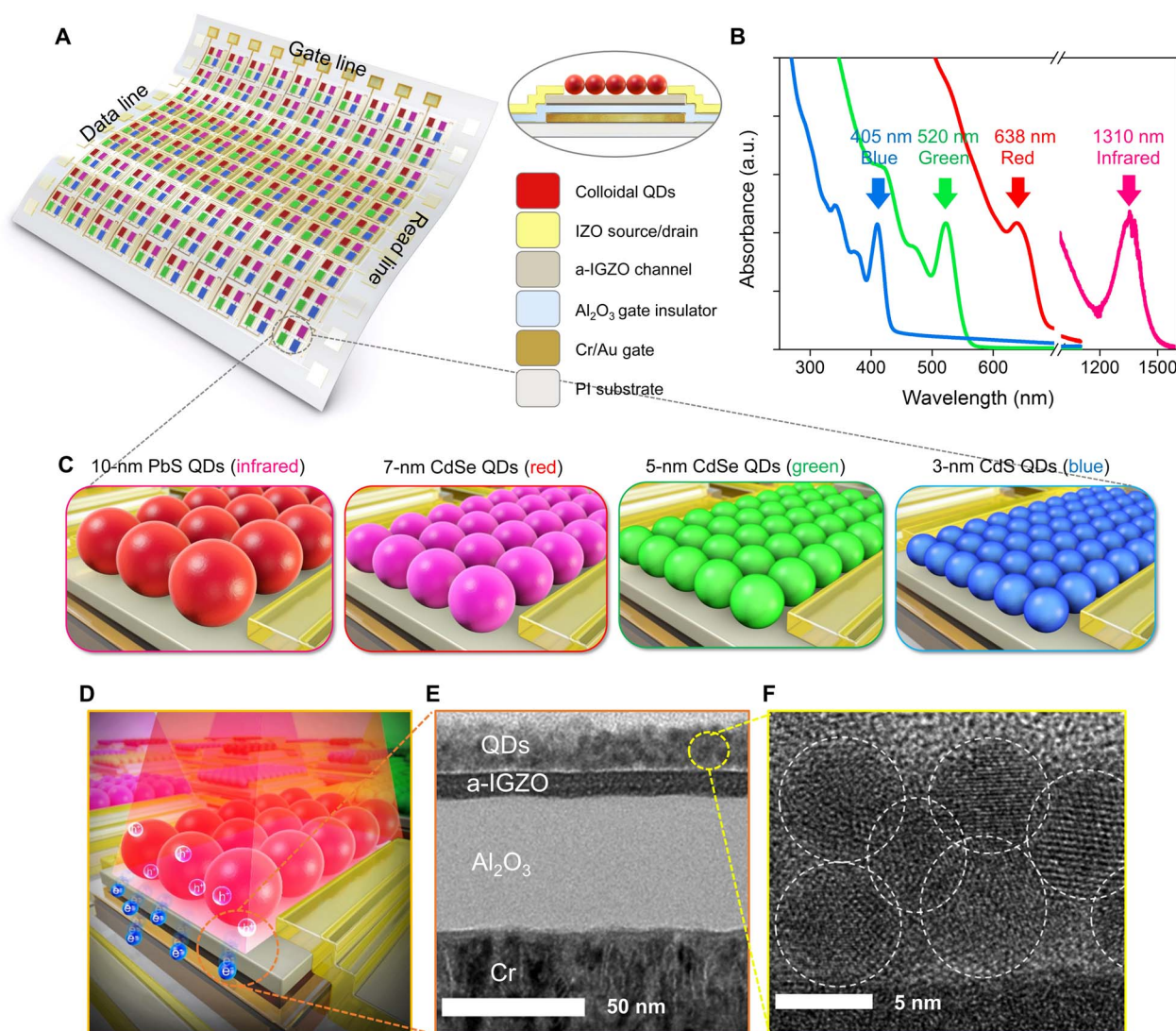
Fig. 1. Schematic of the device structure of the QD/AOS hybrid phototransistor. (**A**) A schematic three-dimensional view of a phototransistor array. (**B**) Optical absorption of QDs used to fabricate the full-color detectors. (**C**) PbS QDs (10 nm diameter), CdSe QDs (7 nm diameter), CdSe QDs (5 nm diameter), and CdS QDs (3 nm diameter) absorb IR, red, green, and blue, respectively. (**D**) Three-dimensional impression image of phototransistor and (**E** and **F**) corresponding cross-sectional HRTEM images. Scale bars, 50 nm (E) and 5 nm (F). a.u., arbitrary units. Photo credit: Jaehyun Kim, Displays and Devices Research Lab. School of Electrical and Electronics Engineering, Chung-Ang University, Seoul 06974, Korea.

pixelized manner (Fig. 1C and fig. S1). Although the semiconducting QDs have been integrated in several optoelectronic devices, including TFTs, because of their inherent tunable bandgaps and high/broad light absorption (Fig. 1B), charge transport is frequently limited by the ligands connecting the QDs (22). On the other hand, a-IGZO TFTs exhibit high electron mobilities (fig. S2), but their photonic performance is limited by low absorption property outside the UV region (fig. S3) (20, 23). However, the synergetic QDs with a-IGZO implementation in the TFT channel, combining a good light absorber that efficiently generates transport electron-hole pairs and a high mobility layer, enable a scalable and high-performance full-color photodetecting device functioning wavelength discrimination from UV to IR light.

Furthermore, the surface structure of QDs, particularly the ligands, strongly affects the charge transfer efficiency of the photogenerated carriers at the QD/a-IGZO interface (22). However, typical QDs have long insulating alkyl chains such as oleic acid as ligands, which substantially impede the charge transfer between the QDs and the a-IGZO film. Thus, to enhance the charge transfer efficiency, a ligand exchange to short and conducting ligands such as ethanedithiol (24), thiocyanate (SCN$^-$) (25), and atomic ligands (26) has been investigated (fig. S4). In addition, there are various chalcometallate ligands for QDs, such as $Sn_2S_6^{4-}$, $Sn_2Se_6^{4-}$, $In_2Se_4^{2-}$, $Cu_7S_4^-$, $Sb_2S_4^{2-}$, $Sb_2Se_4^{2-}$, and CdQ_2^{2-} (Q = Se, Te) to cite a few of them (27). In this study, the critical requirements for ligand choice are stable shell formation and facile electron transport. Considering the stability, accessibility, and sufficient electron transport, we have chosen $Sn_2S_6^{4-}$ as the ideal system among various chalcometallate ligands (28). Furthermore, since SCN$^-$ ligand–based QDs have been widely investigated in high-conductivity/mobility electronic devices, we chose this ligand as the reference in our study. Here, in the case of SCN$^-$-capped QDs, easy decomposition of ligands due to weak monodentate binding results in the formation of sulfur vacancies on the QD surface. These sulfur vacancies can then act as charge-trapping sites, preventing an efficient charge transfer between the QDs and the a-IGZO channel layer. On the other hand, the bidentate $Sn_2S_6^{4-}$ ligands minimize the generation of sulfur vacancies on the QD surface. Overall, the photogenerated electrons from the $Sn_2S_6^{4-}$-capped QDs can be efficiently transferred into the conduction band of the a-IGZO channel layer for charge collection, with minimal trapping events (fig. S5). Also, the photogenerated holes remain in the QDs or near the QD/a-IGZO interface due to the large energy barrier between the valence band maximum of QDs and a-IGZO.

Interfacial properties of QD/a-IGZO phototransistor performance

The optical response characteristics of QD/a-IGZO phototransistors were investigated by using various spectroscopic analyses, such as interfacial trap-related noise analysis and scanning photocurrent microscopy (SPCM). Figure 2 (A and B) shows the noise power spectral density (S_v) of SCN$^-$ and $Sn_2S_6^{4-}$ ligand–capped CdSe QD (7 nm diameter)/a-IGZO phototransistors. According to the interface trapping model for the flicker noise (1/f) analysis, the S_v can be expressed as (29)

$$S_v = (q^2/C_{ox}^2) \cdot (V_D^2/(V_G - V_{th})^2) \cdot ((kT\,D_t)/(LW\ln(\tau_1/\tau_0))) \cdot (1/f) \quad (1)$$

where q is the elementary charge, C_{ox} is the gate oxide capacitance, V_D is the drain voltage, V_G is the gate voltage, V_{th} is the threshold voltage, k is the Boltzmann constant, T is the temperature, D_t is the interface trap

density, L is the length of the channel, W is the width of the channel, f is the frequency, and τ_0 and τ_1 are the minimum and maximum tunneling time, respectively. Here, we assume that $\tau_1/\tau_0 = 10^{12}$ to be consistent with previous work (29, 30), and from the results shown in Fig. 2 (A and B), D_t is estimated as $\sim 4.36 \times 10^{15}$ and $\sim 7.5 \times 10^{12}$ eV^{-1} cm^{-2} for SCN$^-$ and $Sn_2S_6^{4-}$-capped CdSe QD/a-IGZO phototransistors, respectively (at $f = 10$ Hz). It is noted that the SCN$^-$-capped CdSe QD/a-IGZO phototransistor has $\sim 10^3$ times higher trap density than that of the $Sn_2S_6^{4-}$-capped CdSe QD/a-IGZO phototransistor. In particular, the $Sn_2S_6^{4-}$-capped CdSe QD/a-IGZO phototransistor has extremely low trap sites compared with previous works for silicon transistors (31). These results are consistent with the SPCM results, as shown in Fig. 2 (C and D). Here, the total photocurrent and the optical reflectance are measured as a function of the laser position on the phototransistors ($\lambda_{laser} = 532$ nm, power = 0.45 μW, and beam spot size = 500 nm; figs. S6 and S7). The laser is scanned across the source, channel, and drain regions, while measuring the current through the grounded drain electrode. As shown in Fig. 2 (E and F), the $Sn_2S_6^{4-}$-capped CdSe QD/a-IGZO phototransistor exhibits a large Gaussian current profile, showing a photovoltaic-dominated process, while the SCN$^-$-capped CdSe QD/a-IGZO phototransistor shows a clear photothermoelectric response (32). In addition, we observed that the photocurrent level of the $Sn_2S_6^{4-}$-capped phototransistor is much higher than that of the SCN$^-$-capped phototransistor, owing to the efficient transfer of photogenerated electrons from CdSe QDs to the a-IGZO layer, without any charge carrier trapping problem. These results indicate that efficient electron transfer from QDs to a-IGZO is crucial for achieving high photoresponse characteristics.

Figure 3 (A and B) shows the transfer characteristics of SCN$^-$- and $Sn_2S_6^{4-}$-capped CdSe QD/a-IGZO phototransistors under different light intensities. Compared to the SCN$^-$-capped phototransistors, the $Sn_2S_6^{4-}$-capped phototransistors still exhibit low subthreshold slope (SS) and high mobility under light illumination. For instance, at a light intensity of 1.36 mW cm^{-2}, the $Sn_2S_6^{4-}$-capped phototransistors showed SS and mobility of 0.226 V decade^{-1} and 22.01 cm^2 V^{-1} s^{-1}, respectively, while the SCN$^-$-capped phototransistors showed SS and mobility of 0.726 V decade^{-1} and 10.75 cm^2 V^{-1} s^{-1}, respectively. Since the degradation of SS under light illumination can be attributed to the formation of additional trap states, the lower SS value of $Sn_2S_6^{4-}$-capped phototransistors indicates low level of trap states and, consequently, enhanced optoelectronic characteristics (fig. S8). Figure 3 (C and D) compares the photosensitivity (R) and photodetectivity (D^*) of SCN$^-$- and $Sn_2S_6^{4-}$-capped CdSe QD/a-IGZO phototransistors under the white light and broadband illumination (365, 406, 520, 638, and 1310 nm). Here, R and D^* are evaluated by the following equations (13, 15)

$$R = I_{ph}/P, \quad D^* = (A\Delta f)^{1/2}/NEP, \quad NEP = ((\langle I_n^2 \rangle)^{1/2}/R) \quad (2)$$

where I_{ph} is the photocurrent ($I_{ph} = I_{light} - I_{dark}$), P is the light power, A is the illuminated area, Δf is the spectral bandwidth, NEP is the noise equivalent power, and $(\langle I_n^2 \rangle)^{1/2}$ is the root mean square dark noise current from the noise power spectral density. The $Sn_2S_6^{4-}$-capped CdSe QD/a-IGZO phototransistors exhibit extremely high R and D^* values of $\sim 8.3 \times 10^3$ A W^{-1} and $\sim 4.2 \times 10^{17}$ Jones (white light intensity = 1.36 mW cm^{-2}), respectively, compared to those of SCN$^-$-capped phototransistors ($R = \sim 3.1 \times 10^3$ A W^{-1} and $D^* = \sim 5.7 \times 10^8$ Jones). Also, $Sn_2S_6^{4-}$ ligand–based devices showed D^* values of $\sim 1.9 \times 10^{19}$, $\sim 1 \times 10^{18}$, $\sim 7.3 \times 10^{17}$, $\sim 3.6 \times 10^{17}$, and $\sim 1.3 \times 10^{12}$ Jones with UV, blue,
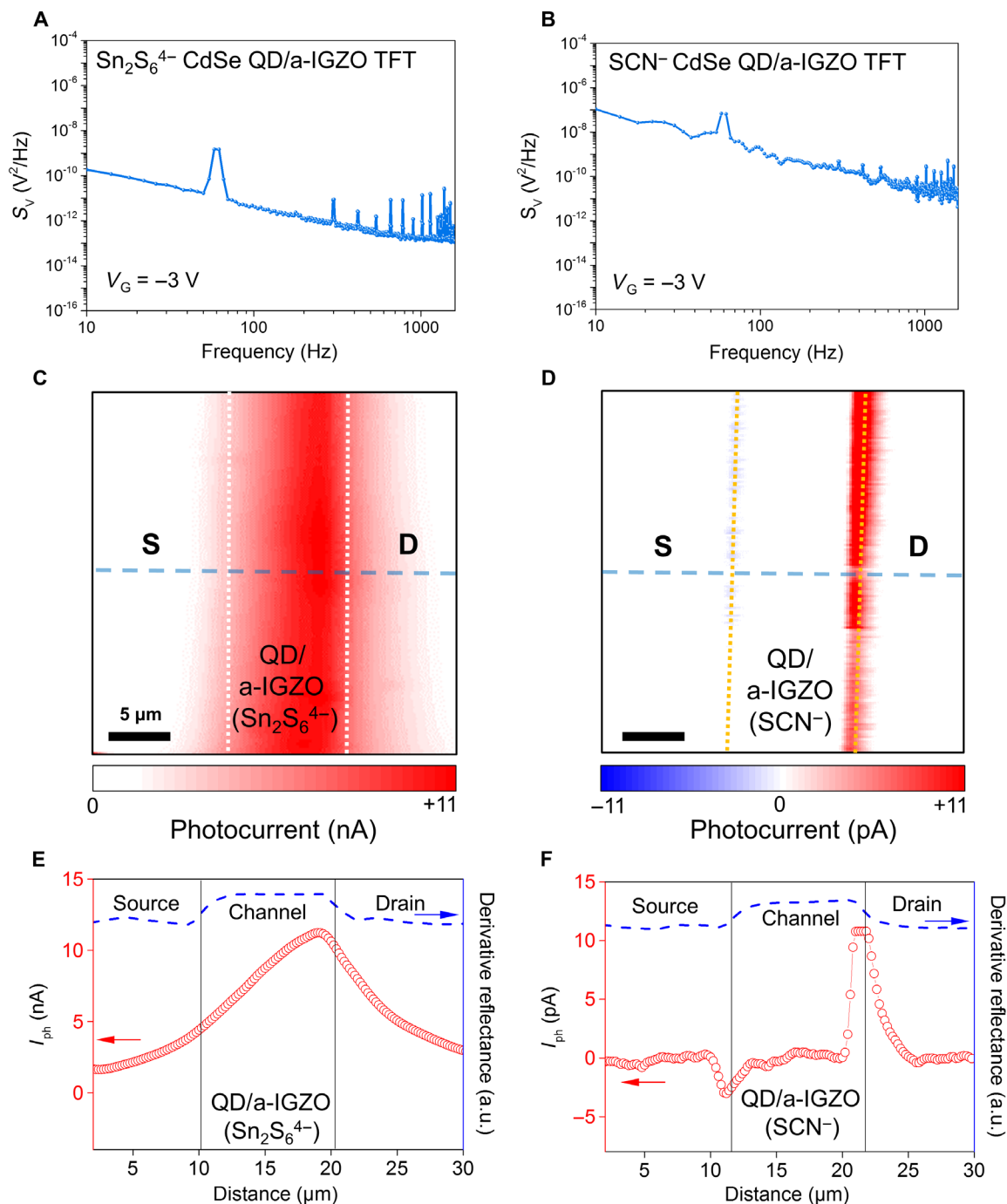
Fig. 2. Interfacial properties between QDs and the AOS channel layer. (**A** and **B**) Noise power spectral density of 7-nm CdSe QD/a-IGZO with SCN⁻ and $Sn_2S_6^{4-}$ ligand phototransistors. (**C** and **D**) Scanning photocurrent imaging (0 V source per drain bias) of the QD/a-IGZO phototransistor with $Sn_2S_6^{4-}$ and SCN⁻ ligands. Scale bars, 5 μm. (**E** and **F**) Photocurrent profile with a laser wavelength of 532 nm and a power of 0.45 μW from along the blue dashed line in (C) and (D). Photo credit: Jaehyun Kim, Displays and Devices Research Lab. School of Electrical and Electronics Engineering, Chung-Ang University, Seoul 06974, Korea.

green, red, and IR irradiation, respectively (fig. S9). These values are about five to six orders of magnitude higher than previous work in the UV range, about four orders of magnitude higher than previous work in the visible range, and about one order of magnitude higher than previous work in the IR range when considering solution-processed organic and QD devices reported to date (*17, 21, 33, 34*). Here, the noise of the device is determined by flicker (1/*f*) noise, which is a resistance fluc-

tuation and always relates to a direct current to avoid overestimating the photodetectivity (*35*). It is argued that such high photoresponse characteristics of $Sn_2S_6^{4-}$-capped phototransistors are attributed to the extremely low 1/*f* noise (~10^{-34} A^2 Hz^{-1}) of the device and the highly conducting and trap-reduced $Sn_2S_6^{4-}$ ligands of our CdSe QDs. Furthermore, the $Sn_2S_6^{4-}$-capped phototransistors exhibit a considerably low off-current level (10^{-13} to 10^{-14} A) and a high illuminated-current
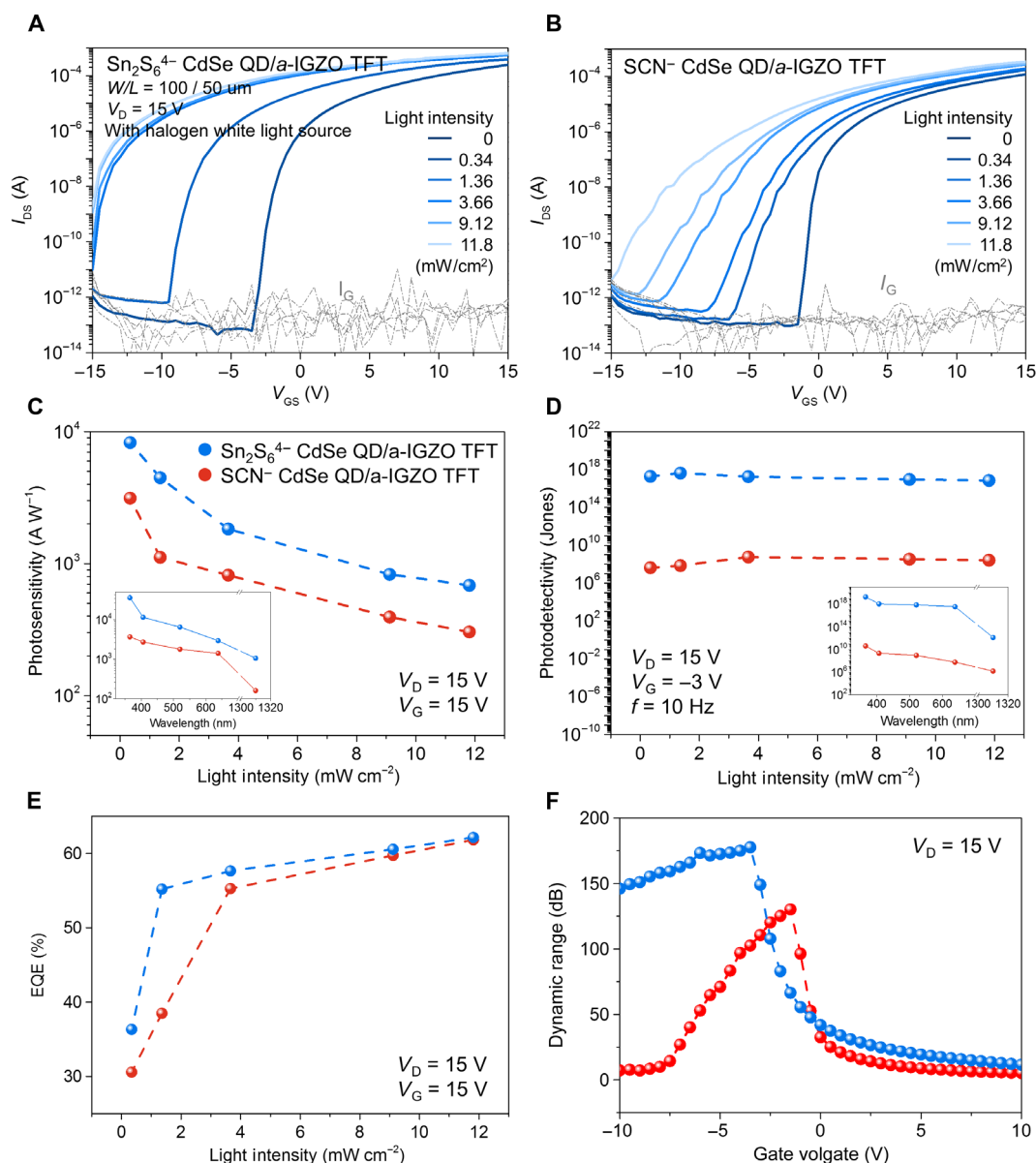
Fig. 3. Optoelectronic performance of the QD/AOS hybrid phototransistor. Photoresponse characteristics of the QD/a-IGZO phototransistor with (**A**) $Sn_2S_6^{4-}$ and (**B**) SCN^- ligands. (**C**) Photosensitivity (R) and (**D**) photodetectivity (D^*) under white light (1.36 mW cm^{-2}) and broadband illumination (inset). Light intensities of UV, blue, green, and red are 1 mW cm^{-2}, while that for IR is 13.6 mW cm^{-2} and that for white light is 1.36 mW cm^{-2}. (**E**) EQE and (**F**) dynamic range of 7-nm CdSe QD/a-IGZO with the $Sn_2S_6^{4-}$ ligand (blue line) and the SCN^- ligand (red line) phototransistor. Photo credit: Jaehyun Kim, Displays and Devices Research Lab. School of Electrical and Electronics Engineering, Chung-Ang University, Seoul 06974, Korea.

level (~10^{-4} A), high EQE (Fig. 3E), wide dynamic range in a broad range of gate bias (>150 dB at V_{GS} = −10 to −2 V, Fig. 3F), and fast photoresponse and decaying behavior (figs. S10). Compared to previous QD phototransistor studies (*15*, *36*) reporting photoresponse times from 0.6 to 0.3 s, our results demonstrate photoresponses of 0.27 s to 90 ms, which are at least three times smaller than those in the literature. Although the speed of our photodetectors remains affected by some trapped charges at the QD interconnections as evidenced from the incident light power–dependent time response of our devices (figs. S11 and S12), the $Sn_2S_6^{4-}$-QD/a-IGZO have shown a much reduced photoresponse time than others, which should be sufficient for photodetector and image-sensing applications.

## High-resolution patterning of QD layers using direct photopatterning

Although the monolithic integration of QDs and AOS layers is pursued to achieve high photoresponse characteristics, high-resolution patterning of QD multiple layers for pixelation is also required to fabricate functional photodetector arrays that guarantee high photodetectivity and wide dynamic range by reducing the leakage currents. Recently, various patterning techniques including inkjet printing, electron beam writing, and transfer printing have been explored for pixelation of QDs (*37*). However, several issues such as limited resolution, poor reliability over a large area, chemical contamination, and fabrication complexity are still problematic. Here, we used a CMOS-compatible direct photopatterning

process to achieve isolated QD layers for sensor arrays without any photoresist, using the high photochemical reactivity of $Sn_2S_6^{4-}$ ligands by UV exposure (fig. S13) such that a photolithography process for pixelation of QD layer is possible. As shown in Fig. 4A, the photochemical reaction of $Sn_2S_6^{4-}$ results in the formation of a stable SnS_2 shell (almost identical optoelectrical performance with $Sn_2S_6^{4-}$ ligands, fig. S14), rather than desorption or decomposition of the ligand, suppressing the formation of anion vacancies and subsequent generation of electron-trapping states. As a result, the UV-exposed region becomes insoluble to dimethyl sulfoxide (DMSO)/ethanolamine (EA) mixed solvent, while the unexposed region remains soluble. In Fig. 4 (B to G), field-enhanced scanning electron microscopy (FESEM) and atomic force microscopy (AFM) images of patterned QD layers confirm the clear patterning of QD layers, having a thickness of ~17 nm (two to three layers of QDs; different types of patterned QDs are also shown in figs. S15 and S16). In addition, the UV-induced photochemical reaction of $Sn_2S_6^{4-}$-capped CdSe QDs is verified by the x-ray photoelectron spectroscopy (XPS) analysis. By the UV exposure, the $Sn_2S_6^{4-}$-capped CdSe QDs exhibit a significant reduction in the normalized S2p peak over the Sn3$d_{5/2}$ peak (from 0.304 to 0.163 after UV exposure), indicating the formation of SnS_2, which corresponds to the theoretical stoichiometry change from $Sn_2S_6^{4-}$ into SnS_2 (fig. S17). Overall, the direct photopatterning of QD layers can effectively reduce the number of

patterning steps and avoid any contact with the photoresist, preventing the degradation caused by the impurity contamination.

Full-color photodetection using an in-pixel CIC

Using the direct photopatterning of various QD layers, a full-color (UV-to-IR) CIC was fabricated (Fig. 5A). Each pixelized QD layer had a pattern size of 40 μm by 100 μm, and the process was repeated to create five different multilayer structures of red (R), green (G), blue (B), and IR QD layers on a-IGZO and a bare a-IGZO for UV detection. The a-IGZO layer is used as channel material for control/switch and wavelength-discriminating integrated circuits. With 600 QD/a-IGZO phototransistors (fig. S18), as shown in Fig. 5 (A and B), in-pixel CIC array is implemented. The schematic of Fig. 5A includes four QD/a-IGZO with $Sn_2S_6^{4-}$ ligand phototransistors [10-nm PbS (T1), 7-nm CdSe (T2), 5-nm CdSe (T3), and 3-nm CdS (T4) QD/a-IGZO TFTs] for IR, R, G, and B detection and two pristine a-IGZO TFTs (T5 and T6; T5, output TFT; T6, driver TFT) for in-pixel amplification circuit and UV detection as well. In particular, the T5/T6 transistor not only enables amplification (fig. S19) but also functions as a UV detector because of the high photoresponsivity of pristine a-IGZO to the UV region. In the dark, there is no transistor response and the lowest output currents correspond to a logic level of (T1 T2 T3 T4 T5; 0 0 0 0 0). Upon IR light illumination, only the T1 transistor activates, resulting in a logic level of
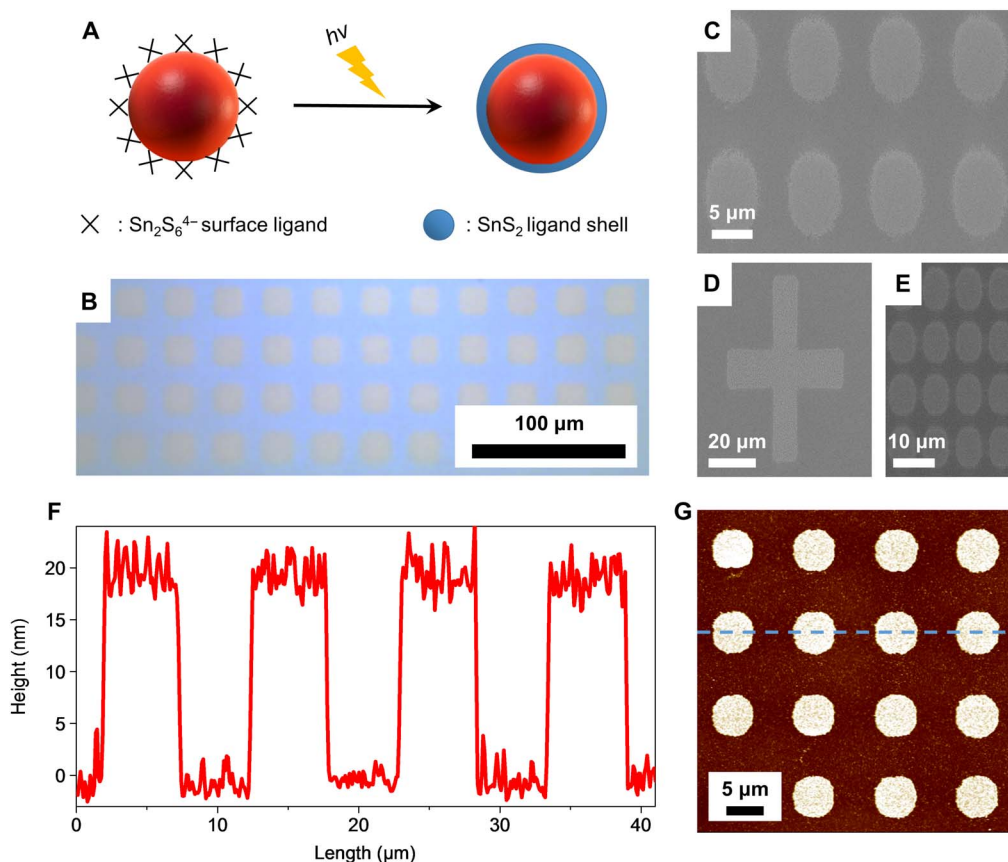
Fig. 4. Fine-patterned QDs characteristics. (**A**) Schematic representation of QDs to design photosensitive inorganic ligands. (**B**) Optical and (**C**) field-enhanced scanning electron microscopy (FESEM) images of patterned CdSe QDs capped with $Sn_2S_6^{4-}$ ligands. (**D**) CdS QDs, (**E**) PbS QDs. Scale bars, 100 μm (B), 5 μm (C), 20 μm (D), and 10 μm (E). (**F** and **G**) Atomic force microscopy (AFM) scan image and height profile of CdSe QDs from along the blue dashed line. Scale bar, 5 μm. Photo credit: Jaehyun Kim, Displays and Devices Research Lab. School of Electrical and Electronics Engineering, Chung-Ang University, Seoul 06974, Korea.

(T1 T2 T3 T4 T5; 1 0 0 0 0). In the cases of red, green, and blue light illuminations, the logic levels of the CIC are (1 1 0 0 0), (1 1 1 0 0), and (1 1 1 1 0), respectively. Upon UV illumination, all transistors activate due to the higher UV optical energy than the bandgap energy of all QDs and a-IGZO; thus, the system exhibits a logic level

of (1 1 1 1 1) and the highest output current (Fig. 5, C to G). By introducing the linear integration of the six phototransistors with a signal-amplification scheme (38), the output current level of the CIC can be associated to a specific wavelength, allowing recognition of various wavelengths of incident light as shown in Fig. 5H (whereas limitation
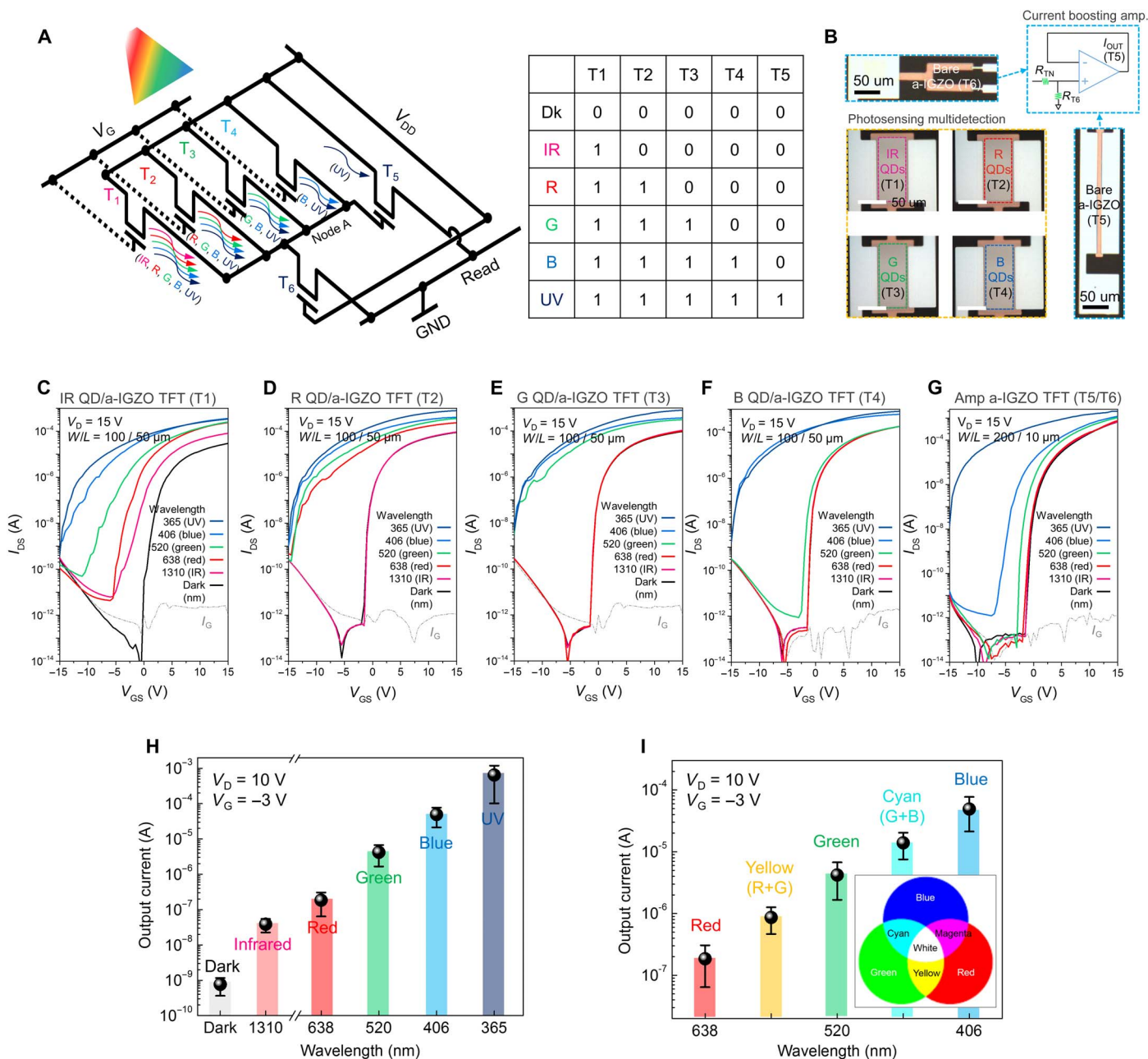
Fig. 5. CIC array characteristics for full-color discrimination. (**A**) Schematic diagram of CIC and logic table of full-color signal detection in one pixel. (**B**) Optical micrograph of the partially patterned QDs including IR PbS (T1, 10 nm), red CdSe (T2, 7 nm), green CdSe (T3, 5 nm), and blue CdS (T4, 3 nm) and bare a-IGZO phototransistors and the schematic of amplification circuit. R_{TN} is the channel resistance of load TFTs (T1 to T4), and R_{T6} is the channel resistance of driver TFT (T6). Here, channel width/length are 100/50 μm (load TFTs), 200/10 μm (T5), and 5/200 μm (T6). Scale bar, 50 μm. (**C** to **G**) Photoresponse characteristics of T1, T2, T3, T4, and T5/T6 with respect to wavelength of light. (**H**) Output current of the five-channel full-color photodetector. (**I**) Mixed light discrimination. Light intensities of UV, blue, green, and red are 1 mW cm^{-2}, while that for IR is 13.6 mW cm^{-2}. For yellow, red (0.5 mW cm^{-2}) and green (0.5 mW cm^{-2}) were mixed, and for cyan, green (0.5 mW cm^{-2}) and blue (0.5 mW cm^{-2}) were mixed. Photo credit: Jaehyun Kim, Displays and Devices Research Lab. School of Electrical and Electronics Engineering, Chung-Ang University, Seoul 06974, Korea.

of color discrimination of a single phototransistor without a CIC circuit is shown in fig. S20). In addition, the wavelength discrimination can be extended to mixed colors such as yellow (R + G) and cyan (G + B) by analyzing the measured output current from the CIC (Fig. 5I and fig. S21). Specifically, from the measured output current levels for red and green light, it is possible to quantify the current level of yellow color between the red and green as shown in Fig. 5I. Similarly, cyan, which is a mixture of green and blue, can be also classified.

A skin-like full-color photodetector array for bio-imaging applications

To demonstrate the possible application of the skin-like full-color photodetector platform, a 10 by 10 multiplexed QD/a-IGZO photodetector array was made on a 3-μm-thick PI substrate for the acquisition of a large amount of position/wavelength-dependent data (Fig. 6, A and B). By using the deep UV (DUV) photochemical activation process (20), the realization of metal oxide–based soft electronics is possible
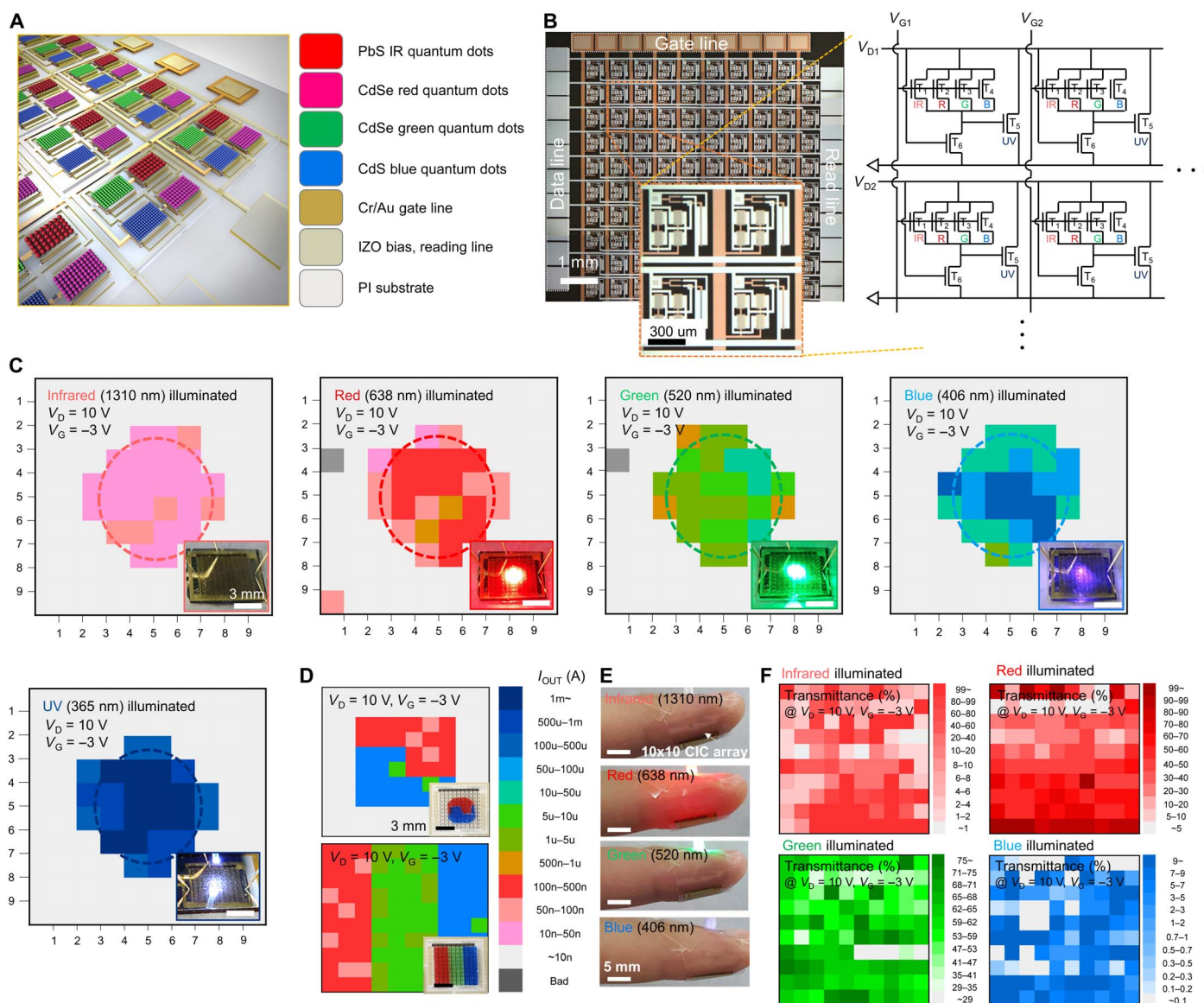
Fig. 6. Full-color two-dimensional mapping applications. (**A**) Schematic illustration of the 10 by 10 CIC array. (**B**) Optical micrograph of the 10 by 10 CIC array on an ultrathin PI substrate and the associated circuit schematic (right). Scale bars, 1 mm and 300 μm (inset). (**C**) Relevant intensity profile reconstructed from output current mapping of the 10 by 10 CIC array on an ultrathin PI substrate with respect to the wavelength of light [IR (1310 nm), R (638 nm), G (520 nm), B (406 nm), and UV (365 nm)]. Light intensities of UV, blue, green, and red are 1 mW cm^{-2}, while that for IR is 13.6 mW cm^{-2}. Scale bar, 3 mm. (**D**) Round and stripe shape two-dimensional mapping images with white light illumination (halogen lamp with 1.36 mW cm^{-2}). Scale bar, 3 mm. (**E**) Photograph of band-type flexible health monitoring system composed of four light sources and phototransistor-based circuit arrays (CIC) attached onto an index fingertip. (**F**) Full-color two-dimensional biological mapping images of human fingertip with respect to the wavelength of light. Light intensities of blue, green, and red are 3 mW cm^{-2}, while that for IR is 13.6 mW cm^{-2}. Each light is placed on the subject's finger, and the transmitted light is collected with the phototransistor-based CIC array placed below the finger. Photo credit: Jaehyun Kim, Displays and Devices Research Lab. School of Electrical and Electronics Engineering, Chung-Ang University, Seoul 06974, Korea.

since the DUV photochemical activation enables the formation of high-performance oxide semiconductors such as IGZO at a low temperature (<150°C). In addition with the low temperature–processed QDs with chalcometallate ligands using nontoxic organic solvents, a multiplexing photodetecting array on an ultrathin PI substrate can be realized, which can be applicable in wearable health care monitoring devices such as an oxygen saturation measurement unit. Here, we observed no significant difference in the photoresponse characteristics in those fabricated on glass and ultraflexible PI substrates (fig. S22). Figure 6C shows the two-dimensional areal mapping of output currents obtained from the photodetector array under illumination of five different light sources (IR, R, G, B, and UV) ($V_G = -3$ V, $V_D = +10$ V). As shown here, although several pixels in the outer region exhibit somewhat deviated current ranges, most of the pixels (yield >99%) show a spatially uniform current distribution to the corresponding light sources. Moreover, position-dependent color mapping is also possible by measuring the R/G/B lights, which are spatially separated from white light (round and strip shapes) (Fig. 6D). Furthermore, for biological applications, particularly for the monitoring of blood oxygen saturation level, the skin-like QD/a-IGZO photodetector array was used to measure the absorption of various wavelengths of light throughout the capillary blood vessels in the index finger (Fig. 6E). The transmission of the light through the blood vessel is varied by the organization of various components such as the bone and tissues, which absorb or scatter light differently. Also, the transmission of the light varies depending on the absorptivity of deoxy- and oxy-hemoglobin in the red blood cells. Figure 6F shows the obtained position-dependent two-dimensionally mapped data for different light sources, showing specific transmittance depending on the wavelength, which is well in agreement with previously reported data (39). The diverse wavelength and position-dependent absorption data may lead to a critical advancement for more reliable and precise diagnostics in health monitoring systems in the near future.

Last, to verify the mechanical and environmental stability of the skin-like QD/a-IGZO photodetector, long-term lifetime and bending/cycling tests were carried out. By passivating the device with a poly(methyl methacrylate) (PMMA) layer having a thickness of ~200 nm, the photosensitivity, photodetectivity, and the photocurrent show only a small variation (<10%) even after 30 days of air exposure compared to the unpassivated devices (fig. S24). In addition, the photoresponse characteristics of the skin-like QD/a-IGZO photodetector was stable under various bending (bending radius down to ~150 μm) and cyclic conditions (0 to 1000 times), without showing any visible mechanical cracks or damages and changes in optoelectronic performances (figs. S25 to S28).

CONCLUSION
In summary, the results presented here argue that low-temperature fabricated diverse QD-based phototransistors and their in-pixel CIC arrays outperform conventional photodiode-based CMOS sensors and current state-of-the art flexible photodetectors, providing full-color photodetection from UV to IR and thereby a general route for highly reliable and conformal two-dimensional photodetectors. The proven synergy of monolithic integration of QDs and AOS phototransistor systems with wavelength discrimination ability can also open new prospect of photodetecting devices and electronics. Photosensitive and high-conductive chelating chalcometallate ligands can perfectly transfer photogenerated electrons to an AOS active layer without electron trapping, resulting in extremely high photosensitivity and photodetectivity. Furthermore, these platforms can be applied to multichannel photosensor arrays due to direct patterning of multiply pixelized QD layers to respond to various stimuli simultaneously and selectively, showing a facile route for various bio-imaging applications.

MATERIALS AND METHODS
Preparation of QDs and chalcometallate ligands
Reagents
Lead acetate trihydrate [Pb(CH$_3$COO)$_2$·3H$_2$O, ≥99.5%], bis(trimethylsilyl) sulfide [((CH$_3$)$_3$SiSSi(CH$_3$)$_3$], sodium sulfide nonahydrate (Na$_2$S·9H$_2$O, ≥98.0%), tin(IV) chloride pentahydrate (SnCl$_4$·5H$_2$O, 98%), oleic acid [CH$_3$(CH$_2$)$_7$CH=CH(CH$_2$)$_7$COOH, 90%], methylammonium chloride (CH$_3$NH$_3$Cl, 98%), and 1-octadecene [ODE; CH$_3$(CH$_2$)$_{15}$CH=CH$_2$, 90%] were purchased from Sigma-Aldrich. Ethanol (C$_2$H$_5$OH, 99.5%), methanol (CH$_3$OH, 99.8%), acetone (CH$_3$COCH$_3$, 99%), and n-hexane (C$_6$H$_{14}$, ≥99%) were purchased from Daejung. CdSe QDs (5 and 7 nm) and CdS QDs (3 nm) in hexane (20 mg/ml) were purchased from Uniam. All reagents were used without further purification.

Ten-nanometer PbS QDs
In a synthesis of PbS QDs, 2 mmol lead acetate trihydrate was mixed with 8 ml of oleic acid and 12 ml of ODE mixture in a 250-ml three-neck flask connected to a Schlenk line. To remove water and volatile impurities, the mixture was heated at 100°C for 2 hours under vacuum. The whole mixture was further heated to 170°C. Separately, an S source solution was prepared by dissolving 1 mmol of bis(trimethylsilyl) sulfide in 10 ml of ODE. The S precursor solution was swiftly injected into the above hot mixture, and the reaction was terminated immediately by removing the flask from the heating mantle. The reaction mixture was naturally cooled down to room temperature. After adding 90 ml of hexane to the reaction mixture, 180 ml of ethanol was added into the solution and centrifuged at 10,000 rpm for 60 min. The colorless supernatant was discarded and the bottom QD precipitate was redispersed in hexane. The process was repeated four times.

(CH$_3$NH$_3$)$_4$Sn$_2$S$_6$
Na$_4$Sn$_2$S$_6$·14H$_2$O (2.325 mmol) and CH$_3$NH$_3$Cl (34.31 mmol) were dissolved in 3 ml of deionized water at room temperature. The solution was stirred at room temperature for 1 hour. The white precipitate was washed with 40 ml of methanol four times. The product was dried under vacuum at room temperature for 1 hour.

Ligand exchange for Sn$_2$S$_6$$^{4-}$-capped QDs
All of the ligand exchange processes were performed in a nitrogen-filled glove box with anhydrous solvents. Five milligrams of chleating chalcometallate capping ligands, such as (CH$_3$NH$_3$)$_4$Sn$_2$S$_6$, was dissolved in 3 ml of the DMSO (99.8%, Sigma-Aldrich)/EA (99.5%, Sigma Aldrich) mixture (2:1 by volume). The solution was added into 2 ml of the oleic acid–capped QDs solution in hexane. After stirring for 3 to 4 hours, the upper colorless hexane part was carefully removed, and the solution was further washed with 2 ml of hexane several times. The ligand exchange QDs solution was mixed with 9 ml of acetonitrile (99.8%, Sigma-Aldrich) and centrifuged at 5000 rpm for 5 min. The upper solution was discarded and the bottom part was redispersed in DMSO/EA mixture solution.

Ligand exchange for SCN$^-$-capped QDs
Five milligrams of ammonium thiocyanate (NH$_4$SCN, 99.99%, Sigma-Aldrich) was dissolved in 1 ml of acetone, and the solution was added into 1 ml of oleic acid–capped QDs solution in hexane. After stirring for

3 to 4 hours, the upper colorless hexane part was carefully removed, and the solution was mixed with 1 ml of tetrahydrofuran (Sigma-Aldrich) and centrifuged at 3000 rpm for 2 min. The upper solution was discarded and the bottom part was redispersed in 1 ml of toluene and centrifuged at 3000 rpm for 2 min. The upper solution was discarded and the bottom part was dispersed in DMSO/EA mixture solution.

Phototransistor device fabrication

PI (15 weight %, Picomax) varnish solution was spin-coated on a glass carrier substrate and annealed at 300°C for 60 min. The PI substrate film had a nominal thickness of 3 μm (measured by a surface profiler). Here, glass substrate was used in the case of glass-based devices. Then, a Cr/Au (5/45 nm) gate electrode was deposited by the evaporator and patterned by using conventional photolithography. On the gate electrode, a 50-nm-thick Al_2O_3 gate insulator layer was deposited using the atomic layer deposition system at 150°C, and IGZO [indium(III) nitrate hydrate $(In(NO_3)_3 \cdot x(H_2O)$, 0.085 M), gallium(III) nitrate hydrate $(Ga(NO_3)_3 \cdot x(H_2O)$, 0.0125 M] and zinc acetate dihydrate $[Zn(CH_3COO)_2 \cdot 2(H_2O)$, 0.0275 M] (all purchased from Sigma-Aldrich) were dissolved in 2-methoxyethanol (anhydrous, 99.8%, Sigma-Aldrich) and stirred for more than 12 hours at 75°C. The channel layer was spin-coated and photochemical activation was followed for 2 hours in a N_2 atmosphere using DUV light (Filgen, UV253H, 18 to 23 mW cm^{-2}). The a-IGZO channel layer and the Al_2O_3 gate insulator layer were patterned using photolithography. Then, a highly conductive indium zinc oxide source/drain with a thickness of 100 nm was deposited using radio-frequency sputtering and patterned using the lift-off process. In addition, the QD layer was spin-coated on top of a-IGZO TFTs and patterned using the direct optical lithography method, followed by annealing at 150°C for 20 min.

Patterning of the QD layer

The QD patterning process was carried out in a clean room via direct optical irradiation with a halogen lamp for 3 min with a quartz photomask. Radiant power is 50 W and beam wavelength is 365 nm (OSRAM HBO 350 W/S). The UV-unirradiated region of the QD layer was rinsed out by DMSO/EA mixture solution so that only the UV-irradiated region remained.

Photoelectronic performance of phototransistors

All electrical and photoresponse characteristics of QD/a-IGZO devices were carried out using Agilent 4156C (Agilent Co.) in air ambient atmosphere at room temperature. For the light source, a white light source (halogen lamp, OSRAM, 64637, 100 W) and a laser source with wavelength centered at 1310-nm (IR), 638-nm (R), 520-nm (G), 406-nm (B) (Thorlabs Co.), and 365-nm (UV) light-emitting diode (LED) were used. The power of white light was measured using a Si photodiode detector (BS-520, S/N 130, Bunkoukeiki Co. Ltd.) and laser/LED were measured using PM100A (Thorlabs Co.). To calculate photosensitivity (R) and the photodetectivity (D^*), the following equations were used (15)

$$R = I_{ph}/P, \, D^* = (A\Delta f)^{1/2}/NEP$$

where I_{ph} is the photocurrent ($I_{ph} = I_{light} - I_{dark}$), P is the light power, A is the illuminated area (channel $W \times L$), Δf is the spectral bandwidth, and NEP is the noise equivalent power. Here, R was extracted from the photoresponse transfer characteristics of the QD/a-IGZO photo-

transistor, and D^* was evaluated using a root mean square dark noise current of $(\langle I_n^2 \rangle)^{1/2}$ from the noise power spectral density measured by using a noise current preamplifier and a vector-signal analyzer. Also, NEP = $((\langle I_n^2 \rangle)^{1/2}/R)$ can be calculated with R of QD/a-IGZO phototransistors at different wavelengths, from the UV to the NIR wavelength region. The frequency/light intensity–dependent D^* was calculated by analyzing the dark noise current in the conducting channel with corresponding optical modulated frequency. Also, EQE was extracted from the following equation (40)

$$R = (\lambda e/hc) \times EQE \times G$$

where R is the photosensitivity, λ is the wavelength, e is the elementary charge, h is the Planck constant, c is the speed of light, and G is the photoconductive gain, which is given by the ratio of carrier lifetime ($\tau_{lifetime}$) over the transit time ($\tau_{transit}$). Furthermore, $\tau_{transit} = L^2/\mu V_{DS}$, where L is the channel length, μ is the carrier mobility, and V_{DS} is the drain-source voltage. Last, dynamic range was expected from the following definition (21)

$$Dynamic \, range = (20 \log (I_{light}/I_{dark}))$$

where I_{light} is the drain current with the light illumination and I_{dark} is the drain current with the dark condition.

SPCM and interfacial trap-related noise analysis

The SPCM was carried out at room temperature in a confocal microscope setup with an objective with a numerical aperture of 0.8. The excitation was provided by a focused laser of a given wavelength (532 nm) and by a supercontinuum white light source (Fianium Ltd) combined with a monochromator for the high-resolution spectra (450 nm ≤ λ ≤ 2000 nm) where λ is the wavelength. During the wavelength scanning, photocurrent is measured by a lock-in technique with a chopper frequency of 500 Hz and subsequently normalized to the photon flux. The chopped laser beam is focused by a microscopic lens (numerical aperture, 0.8) and illuminates the QD/a-IGZO channel and S/D electrode region of devices (32). For the noise measurement, the noise power spectral densities were measured with an SR 570 low–noise current preamplifier (Stanford Research System, Sunnyvale, CA, USA) and an Agilent 35670A dynamic signal analyzer (Agilent Co.).

Characterizations

ζ-Potential measurement

The data were collected using Otsuka ELSZ-1000 (Otsuka Electronics, Japan). Colloidal QD solutions were filled into a quartz cuvette using a flow cell. The measurement was performed without air bubble in the cell.

Fourier transform IR spectroscopy

Fourier transform IR spectra were obtained in the transmission mode using Nicolet 6700 (Thermo Fisher Scientific). The QD films were coated on the intrinsic Si wafer.

X-ray photoelectron spectroscopy

XPS was analyzed with a K-alpha XPS system (ThermoVG Scientific) using a monochromatic Al Kα source at 1486.6 eV and a base pressure of 7.83×10^{-9} mbar.

Absorption spectra

UV-visible–near IR spectroscopy (Cary 5000, Agilent) was used to evaluate the light absorbance of a QD, an a-IGZO film, and a PMMA layer.

Nanostructures of the films

Noncontact AFM (NX10, Park-systems), optical microscopy (BX53M, Olympus), FESEM (SIGMA, Carl Zeiss Co.), and HRTEM (Titan, FEI) were used. The samples were prepared by a Helios 650 (NanoLab) focused ion beam.

SUPPLEMENTARY MATERIALS

Supplementary material for this article is available at http://advances.sciencemag.org/cgi/content/full/5/11/eaax8801/DC1

Fig. S1. Colloidal QD solutions.
Fig. S2. Electrical characteristics of low-temperature photoactivated sol-gel a-IGZO TFTs.
Fig. S3. Absorption spectra of a-IGZO film.
Fig. S4. Synthesis and chemical analysis for chelating chalcometallate ligands ($Sn_2S_6^{4-}$).
Fig. S5. Optoelectronic mechanism of a QD phototransistor.
Fig. S6. SPCM analysis for a QD phototransistor.
Fig. S7. SPCM analysis for an a-IGZO phototransistor.
Fig. S8. Optoelectrical characteristics of a-IGZO TFT and oleic acid-QD/a-IGZO phototransistors.
Fig. S9. Photodetectivity (D^*) of a QD/a-IGZO phototransistor with $Sn_2S_6^{4-}$ and SCN^- ligands as a function of the frequency.
Fig. S10. Photoswitching properties of CdSe QD/a-IGZO phototransistors.
Fig. S11. Temporal response of CdSe QD/a-IGZO phototransistors.
Fig. S12. Temporal photocurrent response of CdSe QD/a-IGZO phototransistors.
Fig. S13. Absorption spectra of chelating chalcometallate ligands.
Fig. S14. Optoelectrical characteristics of CdSe QD/a-IGZO phototransistors before and after QDs patterning.
Fig. S15. Examples of optically patterned QDs.
Fig. S16. HRTEM images of the QDs.
Fig. S17. XPS analysis of CdSe QDs.
Fig. S18. Schematic of direct photolithography process for fine-patterned diverse QD layers.
Fig. S19. In-pixel charge integrating and amplification circuit analysis.
Fig. S20. Limitation of color discrimination of a single phototransistor without a CIC circuit.
Fig. S21. Discrimination of various light wavelength from mixed light.
Fig. S22. Five-channel QD/a-IGZO phototransistors composed of CIC pixel with glass and PI substrate.
Fig. S23. Full-color two-dimensional biological mapping images.
Fig. S24. Long-term reliability test for CdSe QD/a-IGZO with a $Sn_2S_6^{4-}$ ligand phototransistor.
Fig. S25. Ultraflexibility of phototransistor.
Fig. S26. In situ mechanical (bending and cycling) tests for conformal full-color photodetector arrays.
Fig. S27. Photoresponse characteristics of ultraflexible phototransistors.
Fig. S28. Photoresponse characteristics of ultraflexible phototransistors.
References (41–44)

REFERENCES AND NOTES

1. S. Seo, S.-H. Jo, S. Kim, J. Shim, S. Oh, J.-H. Kim, K. Heo, J.-W. Choi, C. Choi, S. Oh, D. Kuzum, H.-S. P. Wong, J.-H. Park, Artificial optic-neural synapse for colored and color-mixed pattern recognition. *Nat. Commun.* **9**, 5106 (2018).

2. Y. Lee, J. Y. Oh, W. Xu, O. Kim, T. R. Kim, J. Kang, Y. Kim, D. Son, J. B.-H. Tok, M. J. Park, Z. Bao, T.-W. Lee, Stretchable organic optoelectronic sensorimotor synapse. *Sci. Adv.* **4**, eaat7387 (2018).

3. T. Yokota, P. Zalar, M. Kaltenbrunner, H. Jinno, N. Matsuhisa, H. Kitanosako, Y. Tachibana, W. Yukita, M. Koizumi, T. Someya, Ultraflexible organic photonic skin. *Sci. Adv.* **2**, e1501856 (2016).

4. S. Goossens, G. Navickaite, C. Monasterio, S. Gupta, J. J. Piqueras, R. Pérez, G. Burwell, I. Nikitskiy, T. Lasanta, E. Galán, E. Puma, A. Centeno, A. Pesquera, A. Zurutuza, G. Konstantatos, F. Koppens, Broadband image sensor array based on graphene–CMOS integration. *Nat. Photonics* **11**, 366–371 (2017).

5. R. D. Jansen-van Vuuren, A. Armin, A. K. Pandey, P. L. Burn, P. Meredith, Organic photodiodes: The future of full color detection and image sensing. *Adv. Mater.* **28**, 4766–4802 (2016).

6. X. Tang, M. M. Ackerman, M. Chen, P. Guyot-sionnest, Dual-band infrared imaging using stacked colloidal quantum dot photodiodes. *Nat. Photonics* **13**, 277–282 (2019).

7. G. Konstantatos, I. Howard, A. Fischer, S. Hoogland, J. Clifford, E. Klem, L. Levina, E. H. Sargent, Ultrasensitive solution-cast quantum dot photodetectors. *Nature* **442**, 180–183 (2006).

8. S. Jeon, S. E. Ahn, I. Song, C. J. Kim, U. I. Chung, E. Lee, I. Yoo, A. Nathan, S. Lee, K. Ghaffarzadeh, J. Robertson, K. Kim, Gated three-terminal device architecture to eliminate persistent photoconductivity in oxide semiconductor photosensor arrays. *Nat. Mater.* **11**, 301–305 (2012).

9. K.-J. Baeg, M. Binda, D. Natali, M. Caironi, Y.-Y. Noh, Organic light detectors: Photodiodes and phototransistors. *Adv. Mater.* **25**, 4267–4295 (2013).

10. M. A. Loi, J. C. Hummelen, Hybrid solar cells: Perovskites under the Sun. *Nat. Mater.* **12**, 1087–1089 (2013).

11. S. M. Kwon, J. K. Won, J.-W. Jo, J. Kim, H.-J. Kim, H.-I. Kwon, J. Kim, S. Ahn, Y.-H. Kim, M.-J. Lee, H.-i. Lee, T. J. Marks, M.-G. Kim, S. K. Park, High-performance and scalable metal-chalcogenide semiconductors and devices via chalco-gel routes. *Sci. Adv.* **4**, eaap9104 (2018).

12. J. Kim, J. Kim, S. Jo, J. Kang, J.-W. Jo, M. Lee, J. Moon, L. Yang, M.-G. Kim, Y.-H. Kim, S. K. Park, Ultrahigh detective heterogeneous photosensor arrays with in-pixel signal boosting capability for large-area and skin-compatible electronics. *Adv. Mater.* **28**, 3078–3086 (2016).

13. I. Hwang, J. Kim, M. Lee, M. W. Lee, H. J. Kim, H. I. Kwon, D. K. Hwang, M. Kim, H. Yoon, Y. H. Kim, S. K. Park, Wide-spectral/dynamic-range skin-compatible phototransistors enabled by floated heterojunction structures with surface functionalized SWCNTs and amorphous oxide semiconductors. *Nanoscale* **9**, 16711–16721 (2017).

14. C. Choi, M. K. Choi, S. Liu, M. S. Kim, O. K. Park, C. Im, J. Kim, X. Qin, G. J. Lee, K. W. Cho, M. Kim, E. Joh, J. Lee, D. Son, S. H. Kwon, N. L. Jeon, Y. M. Song, N. Lu, D. H. Kim, Human eye-inspired soft optoelectronic device using high-density MoS₂-graphene curved image sensor array. *Nat. Commun.* **8**, 1664 (2017).

15. D. K. Hwang, Y. T. Lee, H. S. Lee, Y. J. Lee, S. H. Shokouh, J.-h. Kyhm, J. Lee, H. H. Kim, T.-H. Yoo, S. H. Nam, D. I. Son, B.-K. Ju, M.-C. Park, J. D. Song, W. K. Choi, S. Im, Ultrasensitive PbS quantum-dot-sensitized InGaZnO hybrid photoinverter for near-infrared detection and imaging with high photogain. *NPG Asia Mater.* **8**, e233 (2016).

16. S. Park, S. J. Kim, J. H. Nam, G. Pitner, T. H. Lee, A. L. Ayzner, H. Wang, S. W. Fong, M. Vosgueritchian, Y. J. Park, M. L. Brongersma, Z. Bao, Significant enhancement of infrared photodetector sensitivity using a semiconducting single-walled carbon nanotube/C₆₀ phototransistor. *Adv. Mater.* **27**, 759–765 (2015).

17. K.-S. Cho, K. Heo, C.-W. Baik, J. Y. Choi, H. Jeong, S. Hwang, S. Y. Lee, Color-selective photodetection from intermediate colloidal quantum dots buried in amorphous-oxide semiconductors. *Nat. Commun.* **8**, 840 (2017).

18. J. Bao, M. G. Bawendi, A colloidal quantum dot spectrometer. *Nature* **523**, 67–70 (2015).

19. Y. Shirasaki, G. J. Supran, M. G. Bawendi, V. Bulović, Emergence of colloidal quantum-dot light-emitting technologies. *Nat. Photonics* **7**, 13–23 (2013).

20. Y.-H. Kim, J.-S. Heo, T.-H. Kim, S. Park, M.-H. Yoon, J. Kim, M. S. Oh, G.-R. Yi, Y.-Y. Noh, S. K. Park, Flexible metal-oxide devices made by room-temperature photochemical activation of sol-gel films. *Nature* **489**, 128–132 (2012).

21. A. Pierre, A. Gaikwad, A. C. Arias, Charge-integrating organic heterojunction phototransistors for wide-dynamic-range image sensors. *Nat. Photonics* **11**, 193–199 (2017).

22. M. A. Boles, D. Ling, T. Hyeon, D. V. Talapin, The surface science of nanocrystals. *Nat. Mater.* **15**, 141–153 (2016).

23. J.-W. Jo, Y.-H. Kim, S. K. Park, Light-induced hysteresis and recovery behaviors in photochemically activated solution-processed metal-oxide thin-film transistors. *Appl. Phys. Lett.* **105**, 043503 (2014).

24. E. J. D. Klem, H. Shukla, S. Hinds, D. D. MacNeil, L. Levina, E. H. Sargent, Impact of dithiol treatment and air annealing on the conductivity, mobility, and hole density in PbS colloidal quantum dot solids. *Appl. Phys. Lett.* **92**, 212105 (2008).

25. J. Choi, H. Wang, S. J. Oh, T. Paik, P. Sung, J. S. Jo, X. Ye, T. Zhao, B. T. Diroll, C. B. Murray, C. R. Kagan, Exploiting the colloidal nanocrystal library to construct electronic devices. *Science* **352**, 205–208 (2016).

26. J. Tang, K. W. Kemp, S. Hoogland, K. S. Jeong, H. Liu, L. Levina, M. Furukawa, X. Wang, R. Debnath, D. Cha, K. W. Chou, A. Fischer, A. Amassian, J. B. Asbury, E. H. Sargent, Colloidal-quantum-dot photovoltaics using atomic-ligand passivation. *Nat. Mater.* **10**, 765–771 (2011).

27. M. V. Kovalenko, M. Scheele, D. V. Talapin, Colloidal nanocrystals with molecular metal chalcogenide surface ligands. *Science* **324**, 1417–1420 (2009).

28. S. M. Jung, H. L. Kang, J. K. Won, J. Kim, C. Hwang, K. Ahn, I. Chung, B. K. Ju, M. G. Kim, S. K. Park, High-performance quantum dot thin-film transistors with environmentally benign surface functionalization and robust defect passivation. *ACS Appl. Mater. Interfaces* **10**, 3739–3749 (2018).

29. J. H. D. M. Fleetwood, Physical basis for nondestructive tests of MOS radiation hardness. *IEEE Trans. Nucl. Sci.* **38**, 1567–1577 (1991).

30. X. J. Zhou, D. M. Fleetwood, I. Danciu, A. Dasgupta, S. A. Francis, A. D. Touboul, Effects of aging on the 1/f noise of metal-oxide-semiconductor field effect transistors. *Appl. Phys. Lett.* **91**, 173501 (2007).

31. K. K. Hung, P. K. Ko, C. Hu, Y. C. Cheng, A unified model for the flicker noise in metal-oxide-semiconductor field-effect transistors. *IEEE Trans. Electron Devices* **37**, 654–665 (1990).

32. M.-J. Lee, J.-H. Ahn, J. H. Sung, H. Heo, S. G. Jeon, W. Lee, J. Y. Song, K.-H. Hong, B. Choi, S.-H. Lee, M.-H. Jo, Thermoelectric materials by using two-dimensional materials with negative correlation between electrical and thermal conductivity. *Nat. Commun.* **7**, 12011 (2016).

33. J. S. Lee, M. V. Kovalenko, J. Huang, D. S. Chung, D. V. Talapin, Band-like transport, high electron mobility and high photoconductivity in all-inorganic nanocrystal arrays. *Nat. Nanotechnol.* **6**, 348–352 (2011).

34. T. Shen, J. Yuan, X. Zhong, J. Tian, Dip-coated colloidal quantum-dot films for high-performance broadband photodetectors. *J. Mater. Chem. C.* **7**, 6266–6272 (2019).

35. J. Feng, C. Gong, H. Gao, W. Wen, Y. Gong, X. Jiang, B. Zhang, Y. Wu, Y. Wu, H. Fu, L. Jiang, X. Zhang, Single-crystalline layered metal-halide perovskite nanowires for ultrasensitive photodetectors. *Nat. Electron.* **1**, 404–410 (2018).

36. D. Kufer, I. Nikitskiy, T. Lasanta, G. Navickaite, F. H. L. Koppens, Hybrid 2D–0D MoS2–PbS quantum dot photodetectors. *Adv. Mater.* **27**, 176–180 (2015).

37. Y. Xia, J. A. Rogers, K. E. Paul, G. M. Whitesides, Unconventional methods for fabricating and patterning nanostructures. *Chem. Rev.* **99**, 1823–1848 (1999).

38. J. Kim, J. Kim, K.-T. Kim, Y. Kim, S. K. Park, Monolithic integration and design of solution-processed metal–oxide circuitry in organic photosensor arrays. *IEEE Electron Device Lett.* **37**, 671–673 (2016).

39. S. L. Jacques, Optical properties of biological tissues: A review. *Phys. Med. Biol.* **58**, R37–R61 (2013).

40. D. Kufer, T. Lasanta, M. Bernechea, F. H. L. Koppens, G. Konstantatos, Interface engineering in hybrid quantum dot–2D phototransistors. *ACS Photonics* **3**, 1324–1330 (2016).

41. S. Lany, A. Zunger, Anion vacancies as a source of persistent photoconductivity in II-VI and chalcopyrite semiconductors. *Phys. Rev. B* **72**, 035215 (2005).

42. A. Janotti, C. G. Van De Walle, Oxygen vacancies in ZnO. *Appl. Phys. Lett.* **87**, 122102 (2005).

43. U. Schulz, P. Munzert, R. Leitel, I. Wendling, N. Kaiser, A. Tünnermann, Antireflection of transparent polymers by advanced plasma etching procedures. *Opt. Express* **15**, 13108–13113 (2007).

44. M. S. Park, Y. Lee, J. K. Kim, One-step preparation of antireflection film by spin-coating of polymer/solvent/nonsolvent ternary system. *Chem. Mater.* **17**, 3944–3950 (2005).

Citation: J. Kim, S.-M. Kwon, Y. K. Kang, Y.-H. Kim, M.-J. Lee, K. Han, A. Facchetti, M.-G. Kim, S. K. Park, A skin-like two-dimensionally pixelized full-color quantum dot photodetector. *Sci. Adv.* **5**, eaax8801 (2019).

A skin-like two-dimensionally pixelized full-color quantum dot photodetector

Jaehyun Kim, Sung-Min Kwon, Yeo Kyung Kang, Yong-Hoon Kim, Myung-Jae Lee, Kwangjoon Han, Antonio Facchetti, Myung-Gil Kim and Sung Kyu Park

ARTICLE TOOLS	http://advances.sciencemag.org/content/5/11/eaax8801
SUPPLEMENTARY MATERIALS	http://advances.sciencemag.org/content/suppl/2019/11/18/5.11.eaax8801.DC1
REFERENCES	This article cites 44 articles, 5 of which you can access for free http://advances.sciencemag.org/content/5/11/eaax8801#BIBL
PERMISSIONS	http://www.sciencemag.org/help/reprints-and-permissions

Use of this article is subject to the Terms of Service